Degradation of methyl orange by persulfate activated with magnetically separatable CuFe$_2$O$_4$/RGO nanocomposites: efficiency, stability, and synergy

Zhanmeng Liu[a,*], Xinde Jiang[a], Xianglian Wang[a], Na Sun[b]

[a]*School of Civil Engineering and Architecture, Nanchang Institute of Technology, Nanchang 330099, China, emails: ustblzm@sina.com (Z. Liu), 764556928@qq.com (X. Jiang), wangxianglian@nit.edu.cn (X. Wang)*
[b]*Planning and Design Research Institute, East China Jiao Tong University, 808 East Shuanggang Road, Nanchang 330031, China, email: 821034907@qq.com (N. Sun)*

ABSTRACT

A facile method was used to synthesize CuO/reduced graphene oxide (CuO/RGO), Fe$_3$O$_4$/RGO and CuFe$_2$O$_4$/RGO nanocomposites (NCs) by co-precipitation of graphene oxide (GO) with copper and iron salts in one-pot at 190°C. The structures, compositions, purities, and morphologies of these NCs were analyzed by scanning electron microscopy, X-ray diffraction, X-ray photoelectron spectroscopy, and Fourier transform infrared spectroscopy techniques. The results show that CuO, Fe$_3$O$_4$ and CuFe$_2$O$_4$ nanoparticles decorated uniformly the RGO sheets. The prepared NCs were employed as heterogeneous persulfate activators for the degradation of methyl orange (MO), as a model pollutant. The effects of some key parameters including sodium persulfate (SPS) dosage, activator dosage, initial pH value, and reaction time on MO degradation were investigated. Under the optimized conditions of 5 mM SPS dosage, 1.0 g/L activator dosage at an initial solution pH of 4, 100%, 82.5% and 78.6% of MO could be removed within 90 min in the CuFe$_2$O$_4$/RGO, CuO/RGO and Fe$_3$O$_4$/RGO systems, respectively. The CuFe$_2$O$_4$/RGO NCs exhibited higher efficiency, better reusability and wider pH range for MO degradation than CuO/RGO and Fe$_3$O$_4$/RGO NCs, implying the iron-copper synergy in the material. Especially, the CuFe$_2$O$_4$/RGO NCs exhibited good magnetic separation performance, which favored its recovery and reuse from aquatic environment. The quenching experiments suggest that sulfate radicals were the dominant reactive species.

Keywords: CuFe$_2$O$_4$/RGO composite; Persulfate; Sulfate radical; Graphene oxide; Synergy

1. Introduction

Azo dyes-containing wastewater is characterized by high contents of organic pollutants, complex composition, high chromaticity, strong ecotoxicity, and low biodegradability [1–3]. Thereupon, effective treatment of this wastewater is essential and vital for the environmental protection and human health.

Recently, sulfate radical (SO$_4^{•-}$)-based advanced oxidation processes (SR-AOPs) have become a burgeoning research hotspot and frontier in the field of wastewater treatment due to its advantages such as high redox potential, strong oxidation capacity, high stability, simple operation and no secondary pollution [4]. SR-AOPs were recommended as potential alternatives to hydroxyl radical ($^•$OH)-based AOPs due to the high redox potential of SO$_4^{•-}$ (E^0 = 2.5–3.1 V) relative to that of $^•$OH (1.8–2.7 V) and the wide pH range (4 < pH < 9) [4,5]. Additionally, the longer half-life of SO$_4^{•-}$ (3–4 × 10^{-5} s) than $^•$OH (2 × 10^{-8} s) can render it more opportunities to react with organic pollutants [6].

In general, SO$_4^{•-}$ can be generated by activating persulfate such as peroxymonosulfate and peroxydisulfate

* Corresponding author.

through heat, ultraviolet (UV) radiation, microwave, ultrasonic irradiation, semiconductors, carbon-based catalysts, electro-chemistry, magnetic catalysts, alkaline media or transition metals [7,8]. Among these methods, transition metal-based activation processes are the most simple and convenient technique, with the advantages of low energy consumption and no need for heat and light inputs [4,8]. The principle is that transition metal ions transfer an electron to $S_2O_8^{2-}$, leading to the breakdown of $-O-O-$ bonds of $S_2O_8^{2-}$ and $SO_4^{\bullet-}$ generation as depicted in Eq. (1).

$$S_2O_8^{2-} + M^{n+} \rightarrow SO_4^{\bullet-} + SO_4^{2-} + M^{(n+1)+} \tag{1}$$
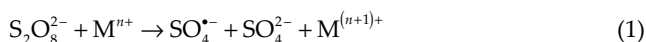
Heterogeneous persulfate activators mainly include metal oxides, composite metal oxides, and metal-free ones [7]. Zero-valent iron (Fe^0), Fe_2O_3 and Fe_3O_4 were widely used as solid heterogeneous activators for SR-AOPs. Fe^0 is a good persulfate activator [9], but it is easy to agglomerate in solution and cannot be regenerated in the treatment process, increasing the treatment cost. Similarly, a large dosage of Fe_2O_3 is required to activate persulfate, and effective activation can only be achieved after transforming Fe^{3+} into Fe^{2+} [10]. As a magnetic iron oxide, Fe_3O_4 contains both Fe^{2+} and Fe^{3+}, and thus Fe^{2+} and Fe^{3+} can be cycled through the redox reaction [11].

The spinel structured ferrites with general formula MFe_2O_4 (M: Mn, Mg, Fe, Co, Ni, Zn, Cu, Cr, etc.) are one of the best nanocatalysts because of their remarkable properties of variety, nanometer size, large specific surface area and superparamagnetic behavior [12,13]. Among the ferrites, copper ferrite ($CuFe_2O_4$) has drawn great attention from scholars to the fields of electronics, biomedicine and various catalysis reactions [14–17]. In these studies, $CuFe_2O_4$ nanoparticles are impressive by the large abundance, low cost, environmental friendliness, high activity, easy recycling and good reusability. However, $CuFe_2O_4$ nanoparticles used as heterogeneous catalysts tend to aggregate in solution due to the ferromagnetic property, leading to lowered performance. Moreover, there is a potential risk of secondary pollution caused by the leaching of excessive Cu^{2+}/Fe^{3+} ions. To overcome the limitations of $CuFe_2O_4$ nanoparticles, reduced graphene oxide (RGO)-supported $CuFe_2O_4$ nanocomposites ($CuFe_2O_4$/RGO NCs) has been widely researched for their use as sensors, catalysts, pollutant adsorbents, supercapacitors, anode material, etc. [18]. Especially, the application of $CuFe_2O_4$/RGO NCs in environmental remediation has attracted wide attention and interests [19–22].

Although the literature are rich with reports on $CuFe_2O_4$/RGO NCs as mentioned above, but few researchers have studied the synergism among CuO, Fe_3O_4 and RGO in persulfate activation. Moreover, the underlying reaction mechanism for azo dye degradation was not yet clearly explored. In the present study, therefore, three NCs, namely CuO/RGO, Fe_3O_4/RGO and $CuFe_2O_4$/RGO, were synthesized by simple solvothermal routes. These composites were characterized by various instrumental methods to deeply reveal and compare their crystal phases, micromorphology, pore structures and surface chemical states, followed by evaluating their functions towards sodium persulfate (SPS) activation for methyl orange (MO) degradation. The recyclability

and stability of the fabricated composites were evaluated in the experiments of SPS activation and MO degradation. The influences of key factors including SPS dosage, activator dosage, solution pH and reaction time on MO degradation were investigated. Radical capture experiments were carried out to analyze the active free radicals playing a major role in the oxidation process.

2. Materials and methods

2.1. Materials and chemicals

All reagents used in this work are of analytical grade or above and used as received. A commercial natural graphite powder (purity > 98%), supplied by Xilong Science Co., Ltd., China, was used as starting material for the preparation of the samples in this work. MO dye ($C_{14}H_4O_3N_3SNa$, purity 99%) was selected as a model compound due to its environmental significance, ease of analysis, and relative solubility in water. Ultrapure water (>18 MΩ) was employed in all experiments.

2.2. Preparation of CuO/RGO NCs

Graphene oxide (GO) was synthesized from natural graphite powder according to the improved Hummers method [23].

CuO/RGO NCs were synthesized by a one-pot solvothermal method. A typical synthesis procedure is as follows: 0.3 g of GO was dispersed in 40 mL of ultrapure water via 1 h of ultra-sonication. Then 0.855 g $CuCl_2·2H_2O$ (5 mmol) was dissolved in the GO dispersion by magnetic stirring for 10 min. Subsequently, 40 mL of freshly prepared NaOH solution (0.5 M) was added dropwise to the reaction mixture to adjust the solution pH exceeding 10, and continuously stirred for 1 h. The whole setup was kept at room temperature. The resultant mixture was transferred to a Teflon-lined stainless steel autoclave and warmed at 190°C in an oven for 10 h under autogenous pressure. After being cooled down to room temperature naturally, the autoclave was taken out from the oven, and the black precipitates were collected by filtration and washed several times with ultrapure water and ethanol, respectively. The product was then dried in a vacuum oven at 60°C for 24 h to acquire the CuO/RGO NCs.

2.3. Preparation of Fe_3O_4/RGO NCs

The preparation process of Fe_3O_4/RGO NCs is similar with that of CuO/RGO NCs with a slight modification. Concretely, 0.3 g of the as-prepared GO was dispersed in 30 mL ethylene glycol under ultrasound for 2 h. Then 1.35 g $FeCl_3·6H_2O$ (5 mmol), 2.46 g sodium acetate (30 mmol) and 0.5 g polyvinylpyrrolidone were added into the above mixture. After stirring for 1 h, the mixture was transferred into a Teflon stainless-steel autoclave and reacted at 190°C for 10 h. The subsequent procedure is identical to the one used for synthesis of CuO/RGO NCs.

2.4. Preparation of $CuFe_2O_4$/RGO NCs

$CuFe_2O_4$/RGO NCs was fabricated following the procedures of Fe_3O_4/RGO synthesization at the same reagent

dosages, except that $CuCl_2 \cdot 2H_2O$ (0.4275 g, 2.5 mmol) and $FeCl_3 \cdot 6H_2O$ (1.35 g, 5 mmol) were added to the reaction mixture to achieve the Cu:Fe molar ratio of 1:2, and the solution pH was adjusted to 10. The preparation process of the $CuFe_2O_4$/RGO NCs is schematically illustrated in Fig. 1.

2.5. Characterization of NCs

X-ray diffraction (XRD) measurements were performed with a Bruker D8 advance diffractometer (Bruker, Germany) with Cu K_α radiation from 5°–80° at a rate of 5°/min. The tube current was 40 mA with a tube voltage of 40 kV. The

Fig. 1. The preparation process of $CuFe_2O_4$/RGO NCs.

average crystallite size was determined through XRD broadening by the Debye-Scherrer formula [24].

X-ray photoelectron spectroscopy (XPS) spectra were acquired with a Thermo Scientific (ESCALAB 250Xi, Thermo, USA) system using monochromatic Al Ka X-ray excitation ($h\nu$ = 1,486.6 eV), operated at working voltage of 15 kV, working current of 50 mA and target power of 400 W.

Scanning electron microscopy (SEM) images were obtained with a JSM-7100F SEM (JEOL, Tokyo, Japan) at 20 kV.

Fourier transform infrared spectroscopy (FT-IR) analysis was conducted on a Nicolet 6700 FT-IR Spectrometer (Thermo-Scientific, USA) under environment condition.

Vibrating sample magnetometer (VSM, model: 7404, Lakeshore, California, USA) was to investigate the magnetic properties at room temperature.

2.6. MO degradation tests

MO degradation tests were conducted in 250 mL conical flasks at 25°C (180 rpm). Firstly, a preformed weight of activators was added with 25 mL ultrapure water, and then the mixture was stirred for 30 min. Afterwards, another 25 mL of MO stock solution (100 mg/L) was added to reach a final concentration of 50 mg/L. After 30-min stirring, the reaction solution reached adsorption–desorption equilibrium. Subsequently, the reactions were initiated by adding preformed volume of SPS solution (1.0 M). Effects of key parameters (i.e., SPS dosage, activator dosage, solution pH and reaction time) on MO degradation were investigated detailed by batch experiments in the same way.

At determined time intervals, 1.0 mL of the suspension was taken out and followed by immediately adding 1.0 mL methanol to quench the reactions. The samples were all filtered through 0.45 μm filters to determine MO concentration by using an ultraviolet-visible spectrophotometer (UV2300II, Tianmei, China) at a wavelength of 464 nm.

Reuse experiments were performed for five times under identical conditions to investigate the stability and sustainability of the NCs. For this, after each run, the NCs were collected by magnet or centrifugation (towards non-magnetic CuO/RGO), washed by ultrapure water and then dried under vacuum oven overnight for use.

Methanol (MeOH) and tert-butanol (TBA) were used as scavengers (at a dosage of 10 mM respectively in the reaction solution) to determine $SO_4^{\bullet-}$ or $^\bullet OH$, respectively, by quenching experiments.

In this work, all the experiments were repeated in triplicate.

3. Results and discussion

3.1. SEM analysis

SEM analysis technique was used to observe the surface physical morphology of the prepared NCs. Fig. 2 displays the SEM images of GO, CuO/RGO, Fe_3O_4/RGO and $CuFe_2O_4$/RGO NCs. The SEM micrograph of GO is shown in Fig. 2a, which exhibits a multi-layer structure with many folds on the surface. This demonstrates that the GO prepared in this work has a high oxidation degree with many layers.
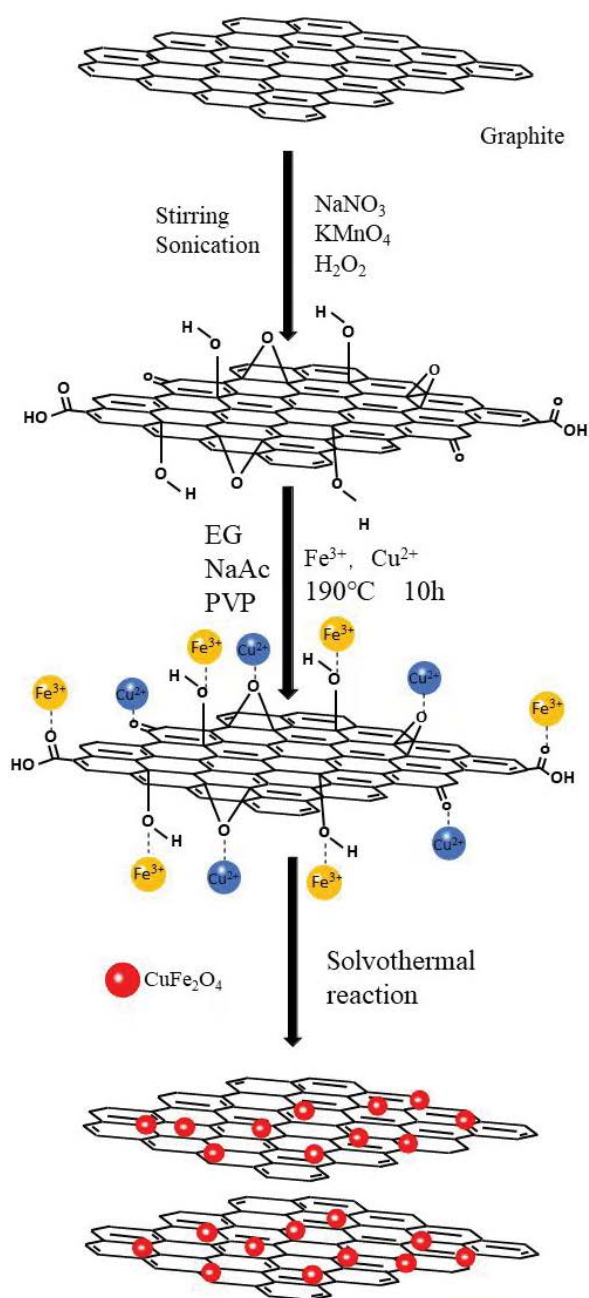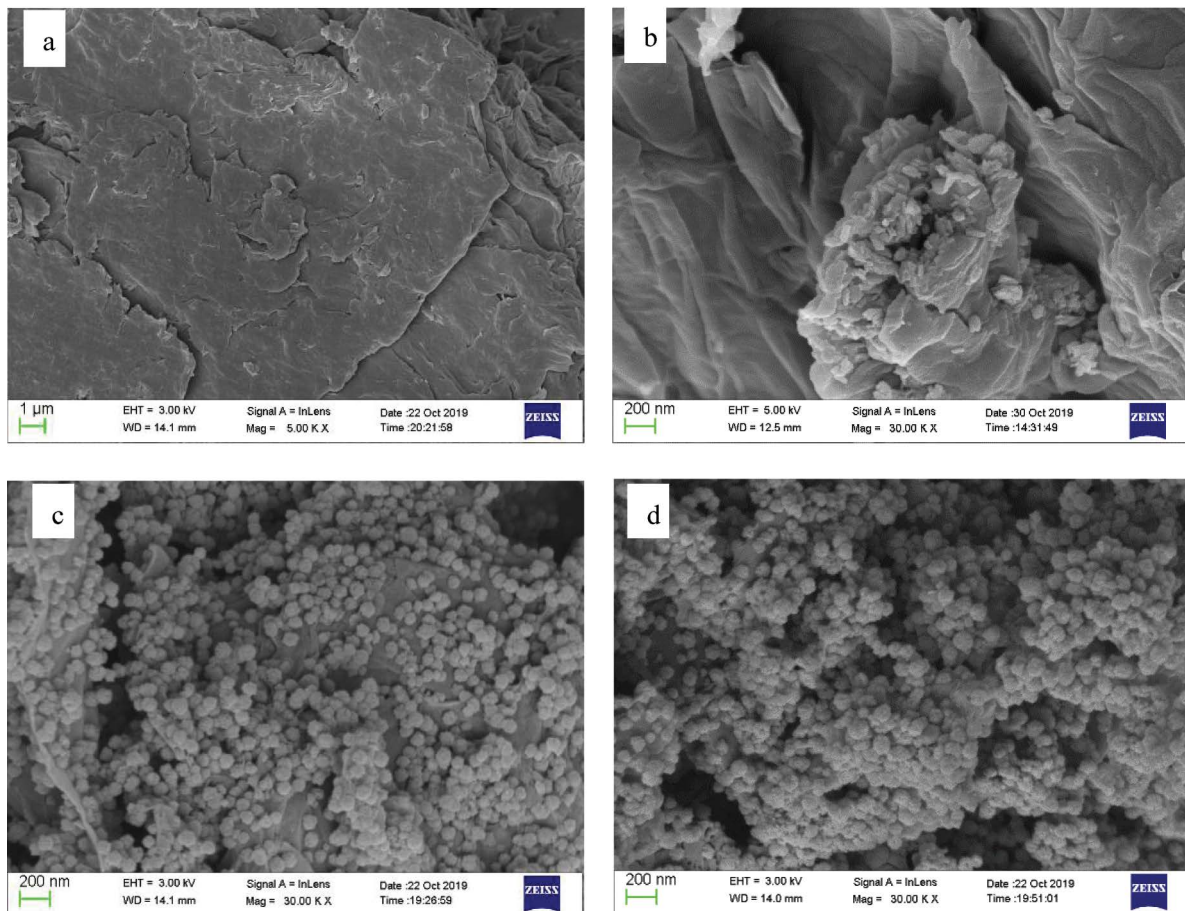
Fig. 2. SEM images of GO (a), CuO/RGO (b), Fe$_3$O$_4$/RGO (c), and CuFe$_2$O$_4$/RGO (d).

As shown in Fig. 2b, CuO was successfully loaded on RGO, and these nanoparticles show irregular spindle shapes with a length of about 120 nm.

It can be seen from Fig. 2c that the Fe$_3$O$_4$ nanoparticles have a regular spherical shape, uniform particle size and relatively uniform distribution on the RGO sheets. This demonstrates that the interaction between Fe$_3$O$_4$ nanoparticles and RGO surface is strong. Moreover, the folds of RGO can be seen from Fig. 2c. This morphology can effectively prevent the agglomeration of Fe$_3$O$_4$ nanoparticles, and the existence of Fe$_3$O$_4$ nanoparticles can also avoid the superposition of RGO sheets.

Fig. 2d shows that CuFe$_2$O$_4$ nanoparticles are predominantly spherical and evenly distributed onto the RGO sheets. Although the product has been washed with water and ethanol repeatedly after preparation, most of the particles still exist on the surface of RGO sheets (Fig. 2d). This indicates that the prepared product was stable and there was a strong interaction between CuFe$_2$O$_4$ nanoparticles and RGO sheets.

3.2. XRD analysis

The XRD patterns of the bare GO, and as-fabricated CuO/RGO, Fe$_3$O$_4$/RGO and CuFe$_2$O$_4$/RGO NCs are shown in Fig. 3. A strong diffraction peak at $2\theta = 10.6°$ indicates the existence of layered structure in GO, corresponding to the (001) crystalline plane of GO. The weak diffraction peaks at $2\theta = 26.0°$ and 44.0° of GO are attributed to incomplete oxidation or impurities, but their intensity is much lower than that of GO characteristic peak ($2\theta = 10.6°$) (Fig. 3). This case demonstrates the successful preparation and good crystallinity of GO. After GO and CuO recombination, the peak at $2\theta = 10.6°$ disappears, whereas a new peak (25.6°) assigned to the (002) crystalline plane of RGO occurs. This indicates that GO was reduced to RGO during hydrothermal preparation. The XRD pattern of CuO/RGO shows obvious characteristic diffraction peaks at $2\theta = 32.8°$, 35.8°, 39°, 49°, 58.7°, 61.7°, 66.4° and 75.4° (Fig. 3). These peaks can be ascribed to the diffraction lines produced by (110), (–111), (111), (–202), (202), (–113), (–311) and (–222) crystalline planes of the end-centered monoclinic structured CuO (JCPDS card no. 89-5895) [25]. No peaks from other phases were detected, indicating the high purity of the product.

The main peaks of Fe$_3$O$_4$/RGO located at 18.5°, 30.3°, 35.7°, 36.7°, 43.4°, 53.8°, 57.4°, 62.5°, 71.4° and 74.5° (Fig. 3) for two theta correspond to crystal planes of (111), (220), (311), (222), (400), (422), (511), (440), (620) and (533), respectively, of Fe$_3$O$_4$ with cubic spinel structure (JCPDS No: 19-0629) [26,27]. Moreover, there are no other impurity peaks in the XRD graph of Fe$_3$O$_4$/RGO, indicating the high purity of the prepared Fe$_3$O$_4$ nanoparticles. Applying the

Debye–Scherer equation [24], the average crystallite size of Fe_3O_4 was calculated to be 21 nm.

As for the pattern of $CuFe_2O_4$/RGO, the diffraction peaks at 2θ = 18.3°, 30.3°, 35.7°, 36.5°, 43.5°, 50.7°, 53.9°, 57.4°, 63.1°, 71.7° and 74.5° can be indexed to the (101), (200), (211), (202), (220), (204), (312), (303), (400), (332), and (413) planes of cubic $CuFe_2O_4$ (JCPDS 34–0425) (Fig. 3). The average size of Fe_3O_4 particles is 45 nm (estimated by the Debye–Scherrer equation). These results are in agreement with the results reported in the literature [19–22], indicating the successful preparation of $CuFe_2O_4$/RGO NCs. In addition, the diffraction peaks have high intensity, and there are almost no other impurity peaks, indicating that the prepared $CuFe_2O_4$/RGO NCs are of high purity. Moreover, like CuO/RGO and Fe_3O_4/RGO, the peak at 2θ = 10.6° vanishes, and the (002) crystalline plane peak of RGO appears at 2θ = 25.6°. The weak intensity of the peak at 2θ = 25.6° can be ascribed to the shielding of strong diffraction peaks of $CuFe_2O_4$. It can also be seen from the SEM image (Fig. 2d) that a large number of $CuFe_2O_4$ nanoparticles are loaded on the surface of RGO.

3.3. FT-IR analysis
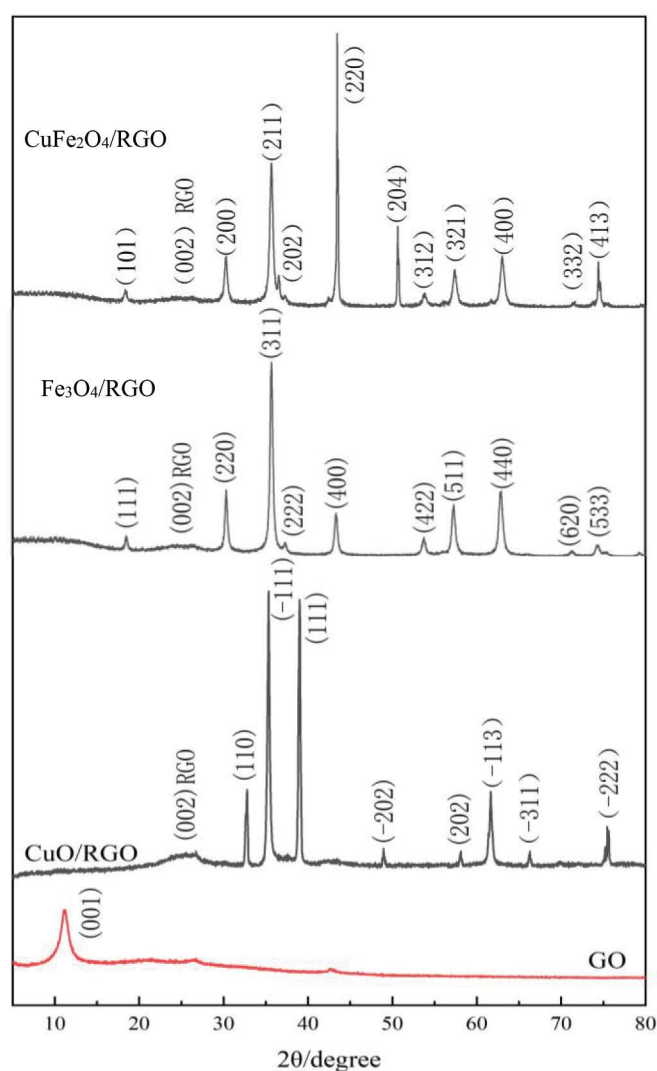
To obtain insights into the chemical structures of GO, CuO/RGO, Fe_3O_4/RGO and $CuFe_2O_4$/RGO, FT-IR spectroscopy was employed to study the existence of oxygen-containing functionalities and their changes after recombination (Fig. 4). It can be found that the strongest absorption peak appears at 3,438–3,445 cm^{-1} in the four spectra. These bands are attributed to the stretching vibration of O–H and/or water molecules [28]. In the FT-IR spectrum of GO, the peaks at 1,722; 1,622; 1,244 and 1,060 cm^{-1} corresponded to the stretching vibration of C=O (COOH), C=C (C–C), C–O–C and C–O functional groups, respectively (Fig. 4) [29].

The peak at 1,722 cm^{-1} (C=O) disappears in the FT-IR spectra of CuO/RGO, Fe_3O_4/RGO and $CuFe_2O_4$/RGO (Fig. 4). The peak at 1,060 cm^{-1} (C–O) also disappears in the FT-IR spectrum of CuO/RGO, and its intensity attenuates in the FT-IR spectra of Fe_3O_4/RGO and $CuFe_2O_4$/RGO. This result suggests that during the preparation of the NCs, a large number of oxygen-containing functional groups in GO disappeared and GO was reduced to RGO. In the CuO/RGO spectrum, two peaks emerge at 1,646 and 1,165 cm^{-1}, corresponding to the stretching vibration of C=C and C–O–C, respectively. In addition, new peaks were observed at 1,558 and 1,572 cm^{-1} in the CuO/RGO and $CuFe_2O_4$/RGO spectra, respectively, which can be indexed to the skeleton vibration of graphene sheets. The absorption peak of CuO/RGO spectrum at 618 cm^{-1} belongs to the characteristic peak of CuO. In the Fe_3O_4/RGO

Fig. 3. XRD patterns of GO, CuO/RGO, Fe_3O_4/RGO and $CuFe_2O_4$/RGO NCs.
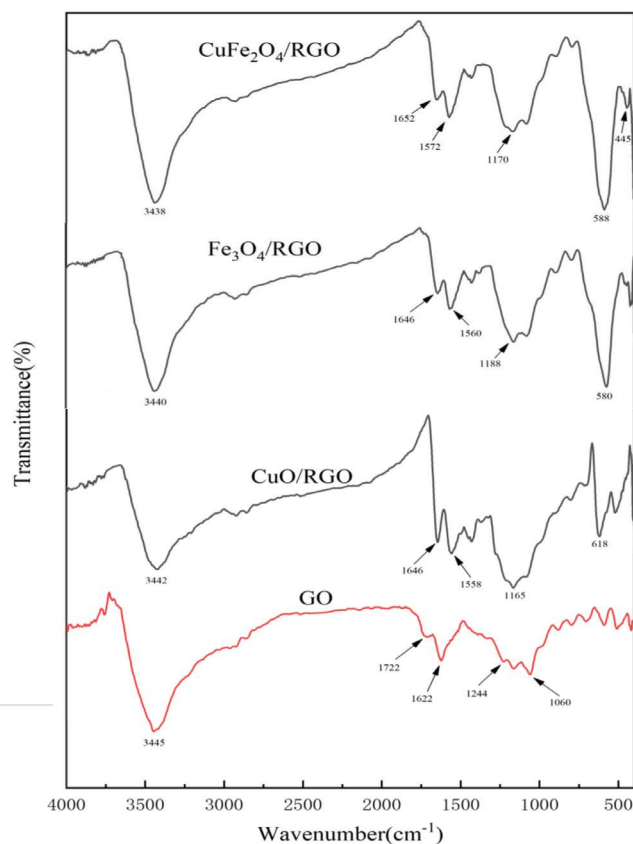
Fig. 4. FT-IR spectra of GO, CuO/RGO, Fe_3O_4/RGO and $CuFe_2O_4$/RGO NCs.

and CuFe$_2$O$_4$/RGO spectra, the peak at 580–588 cm^{-1} verifies the formation of Fe–O bond with tetrahedral geometry in spinel-type complexes [30]. Moreover, the peak at 445 cm^{-1} in the CuFe$_2$O$_4$/RGO spectrum represents the tensile vibration of Cu–O in octahedral-type complexes. The emergence of these characteristic peaks confirms the existence of Fe^{3+} and Cu^{2+} in tetrahedral and octahedral coordination environments, respectively, implying that the nanoparticles were decorated on the RGO sheets. And these results are consistent with that of SEM and XRD analyses.

3.4. XPS analysis

XPS measurement was conducted to detect the chemical composition of CuFe$_2$O$_4$/RGO NCs. Fig. 5a shows the existences of Cu, Fe, O and C in CuFe$_2$O$_4$/RGO NCs, and no other impurities were detected. Fig. 5b demonstrates the Cu 2p spectrum, which can be resolved into two peaks, located at 933 eV for Cu 2p$_{3/2}$ and at 952.8 eV for Cu 2p$_{1/2}$, both of which are indexed to ≡Cu^{2+} [21]. Fig. 5c shows the Fe 2p XPS spectrum, in which the broad peaks at 711.3 and 724.6 eV are assigned to Fe 2p$_{3/2}$ and Fe 2p$_{1/2}$, which are ascribed to ≡Fe^{2+} and ≡Fe^{3+} [21]. In addition, the satellite peak signal at 719.1 eV further confirms the presence of Fe^{3+}. The spectrum of C 1s shows three peaks at 287.8, 286.2 and 284.7 eV, which are attributed to the bonds of HO–C–O, C–O and C–C, respectively (Fig. 5d). These are the typical functional groups of RGO. Moreover, the intensity of HO–C–O (287.8 eV) and C–O (286.2 eV) characteristic peaks is apparently lower than that of C–C (284.7 eV). This shows that during the preparation of the NCs, most of the oxygen-containing groups on the original GO were reduced and GO was reduced to RGO in the hydrothermal process. XPS spectrum of O 1s is depicted in Fig. 5e, wherein one peak at 530.3 eV corresponds to lattice oxygen O of Cu–O and Fe–O groups and the other peaks at 531.5 and 532.7 eV can be attributed to the surface O–H and C–O groups respectively. In conclusion, the results of XPS analysis are in accordance with that of XRD, indicating the successful preparation of high-purity CuFe$_2$O$_4$/RGO NCs.

3.5. VSM measurement

The magnetic property of catalysts is important for recyclable utilization in wastewater treatment. As shown in Fig. 6, the samples of Fe$_3$O$_4$/RGO and CuFe$_2$O$_4$/RGO display the symmetrical S-shaped of magnetization curves, suggesting the nanosized dimension and the superparamagnetic behavior of the samples. Both the coercive force and remanent magnetization of the materials are zero, indicating that the NCs are of superparamagnetism. The saturation magnetization value of CuFe$_2$O$_4$/RGO (42.9 emu/g) is smaller than that of Fe$_3$O$_4$/RGO (51.26 emu/g) (Fig. 6a and b), which can be due to the presence of the non-magnetic Cu in the complex. Nevertheless, the digital picture inserted in Fig. 6b shows that CuFe$_2$O$_4$/RGO NCs were efficiently separated within 20 s under the external magnetic field, verifying the good magnetic separation property of the as-fabricated material. When the external magnet was removed, the stable suspended solution was formed again. These results suggest that the prepared composites have good

recycling property, which is beneficial for the recovery of the materials from aqueous environment and for preventing the water from secondary pollution after reaction.
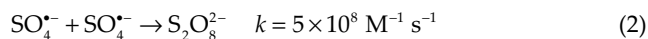
3.6. MO degradation by SPS activation with various activators

To comprehensively evaluate the catalytic performance of CuFe$_2$O$_4$/RGO, a series of side-by-side experiments were conducted using different activators (CuO/RGO, Fe$_3$O$_4$/RGO and CuFe$_2$O$_4$/RGO). For this, the influences of several operating parameters, including SPS dosage, activator dosage, solution pH and reaction time for MO degradation were systematically investigated through single factor experiments.

3.6.1. Influence of SPS dosage

The dosage of oxidants is an important factor affecting the treatment effect of oxidation systems. The cost of oxidants is also an expensive item in practical application. Therefore, it is very necessary to find an optimal dosage of oxidants.

The influence of SPS dosage ([SPS]$_0$) on MO removal was studied at 1–6 mM, while activator dosage = 1.0 g/L, solution pH = 4, reaction time = 120 min. Fig. 7a depicts the effect of SPS dosage on MO removal efficiency in the CuO/RGO, Fe$_3$O$_4$/RGO and CuFe$_2$O$_4$/RGO systems with other factors fixed. It can be seen that the removal efficiencies of MO by CuO/RGO, Fe$_3$O$_4$/RGO and CuFe$_2$O$_4$/RGO without oxidant SPS were 16.4%, 14.4% and 19.6%, respectively, which can be attributed to the adsorption effect of the activators. The same as one expected, under 120 min reaction, when SPS dosage is raised from 1 to 5 mM, the degradation ratio of MO increases from 51.1%, 56.1% and 59.5% to 84.0%, 80.3% and 100% in the CuO/RGO, Fe$_3$O$_4$/RGO and CuFe$_2$O$_4$/RGO systems, respectively, but slight improvement and even reduction is measured at [SPS]$_0$ > 5 mM (Fig. 7a). For example, MO degradation efficiency decreases from 84.0% to 78.6% when [SPS]$_0$ increases from 5 to 6 mM in the CuO/RGO system. Notably, significant improvement in MO degradation is observed with increasing [SPS]$_0$ to 4 mM, indicating the SPS-driven formation of SO$_4^{•-}$ radicals. It can be speculated that the generation of more SO$_4^{•-}$ contributes to the greater MO degradation at higher SPS dosages. Similar results were also reported by others [20,21]. In this work, the MO removal ratio is not proportional to SPS dosage (Fig. 7a), which can be attributed to the quenching of SO$_4^{•-}$ by self-coupling reaction or residual S$_2$O$_8^{2-}$ [Eqs. (2) and (3)] [22,31]. Hao et al. [22] even observed decreased degradation efficiency at higher SPS dosages.

$$SO_4^{•-} + SO_4^{•-} \rightarrow S_2O_8^{2-} \quad k = 5 \times 10^8 \ M^{-1} \ s^{-1} \tag{2}$$

$$SO_4^{•-} + S_2O_8^{2-} \rightarrow S_2O_8^{•-} + SO_4^{2-} \quad k = 1 - 6.1 \times 10^6 \ M^{-1} \ s^{-1} \tag{3}$$

3.6.2. Influence of activator dosage

The removal of MO at different activator dosages was investigated in this study under the conditions of SPS dosage = 5 mM, solution pH = 4, reaction time = 120 min. For comparative purposes, the adsorption amounts of MO by
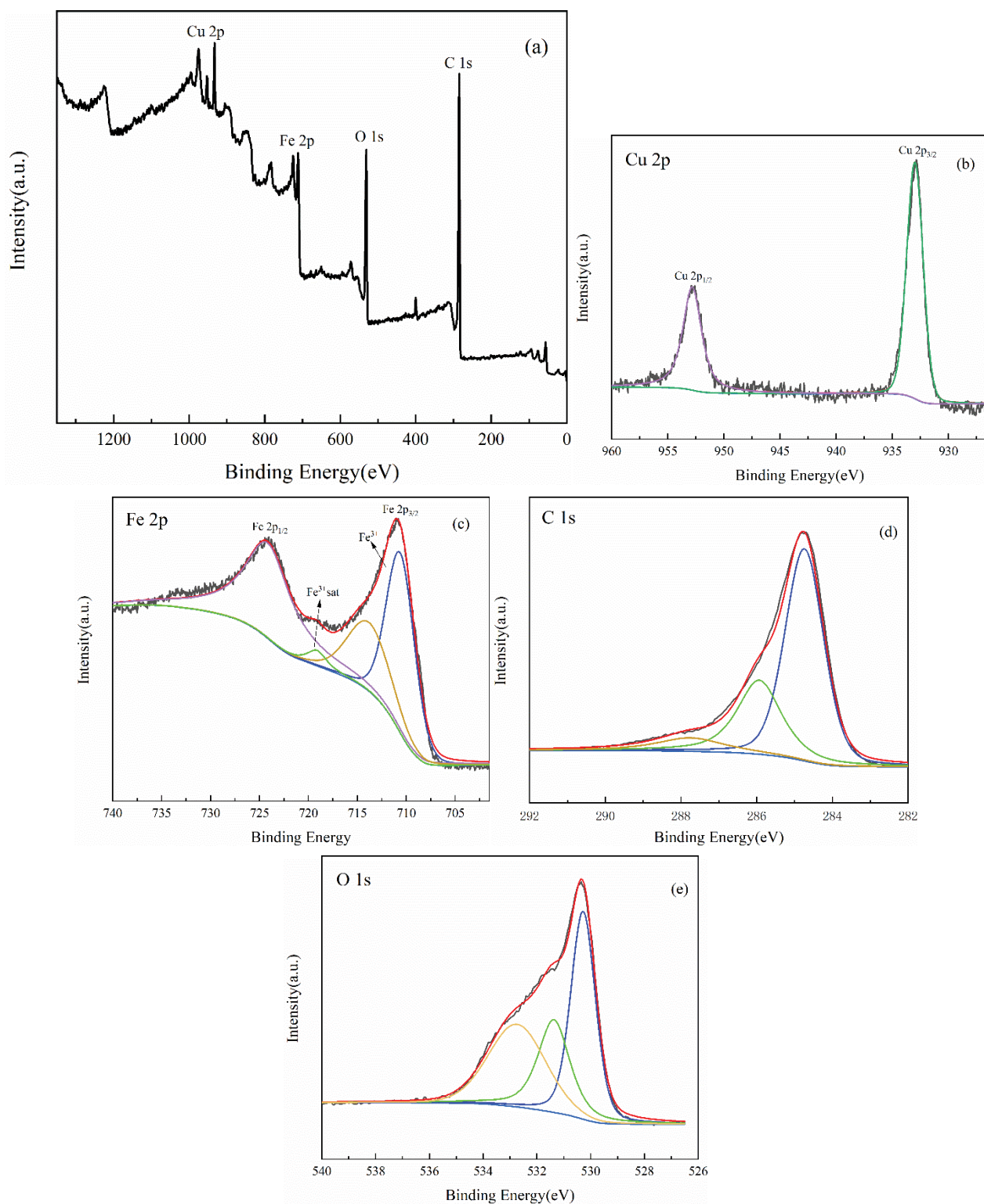
Fig. 5. XPS spectra of fresh $CuFe_2O_4$/RGO NCs: (a) survey spectra, (b) Cu 2p, (c) Fe 2p, (d) C 1s, and (e) O 1s.

the activators have been deducted from the removal ratios. As illustrated in Fig. 7b, SPS only results in 18.3% removal for MO in 120 min without any activator. This is because that SPS itself is an oxidant with certain oxidative capacity towards dyes [32]. However, due to the lack of activation,

the degradation efficiency of MO by SPS alone is low. The removal efficiency of MO is improved with activator dosage increasing from 0.2 to 1.0 g/L (Fig. 7b). MO removal efficiency reaches 100% in the $CuFe_2O_4$/RGO system, which is higher than the CuO/RGO (84.0%) and Fe_3O_4/RGO (80.3%)
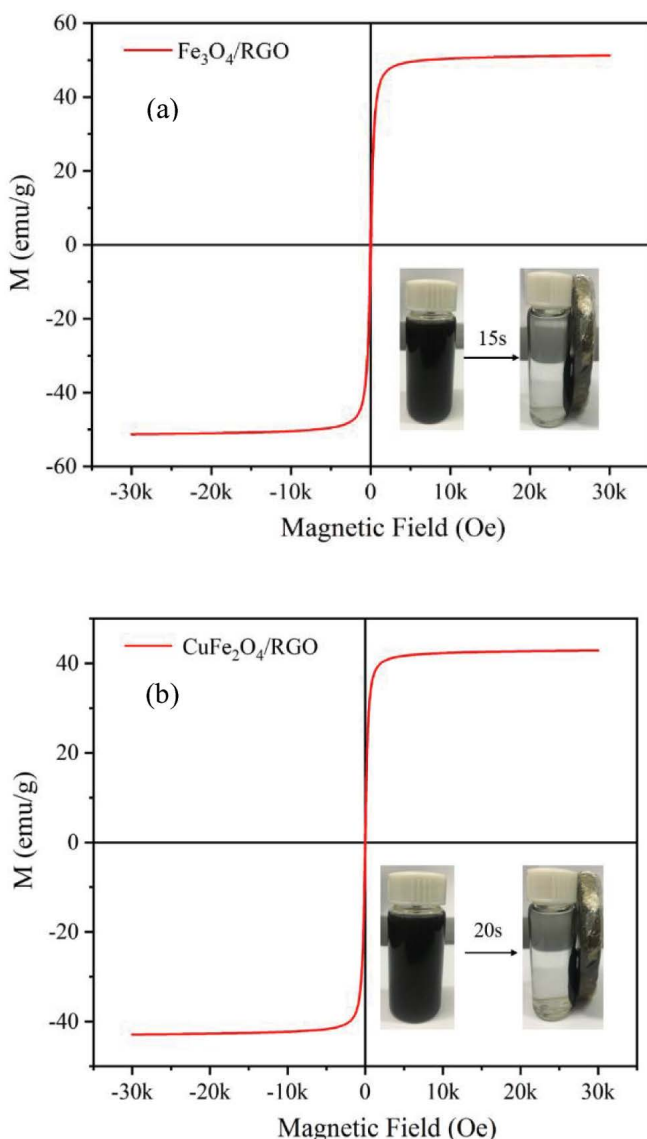
Fig. 6. Magnetic hysteresis loops of prepared Fe₃O₄/RGO (a) and CuFe₂O₄/RGO (b) NCs.

systems. Thereupon, CuFe₂O₄/RGO was more effective in activating SPS than CuO/RGO and Fe₃O₄/RGO for MO degradation. The enhanced degradation efficiency at high activator dosages is largely attributed to the increased number of active sites on the activator surface, which can catalyze SPS to generate more radicals [15]. Nevertheless, in this work, a mild increment and even a decrease are found in MO removal when the activator dosage is increased from 1.0 to 1.2 g/L (Fig. 7b), because the excess dosing of activators can quench the reactive radicals. On the basis of these results, 1.0 g/L was selected as the optimum activator dosage and employed in the following experiments.

3.6.3. Influence of initial solution pH

Solution pH is a key factor in water remediation by SR-AOPs because of the role of pH in controlling the activity

of oxidants and the substrates. Fig. 7c shows the influence of initial solution pH on MO removal under the conditions of SPS dosage = 5 mM, activator dosage = 1.0 g/L, reaction time = 120 min. As can be clearly seen, the catalytic activity of three activators is significantly higher in the acidic medium compared to the basic medium. In the CuO/RGO system, highly acidic (pH 2) and alkaline solution (pH 8–10) show apparently negative effects on MO degradation, whereas MO removal is maximized at pH 4; in the Fe₃O₄/RGO and CuFe₂O₄/RGO systems, the MO removal ratio is similar between pH 2 and 4, and the degradation performance gradually declines with increasing pH from 4 to 10 (Fig. 7c). Moreover, the change range of MO removal ratio in the CuFe₂O₄/RGO system with altering solution pH is less than that in the CuO/RGO and Fe₃O₄/RGO system, suggesting that the heterogeneous catalyst CuFe₂O₄/RGO can activate SPS over a wide pH range. Under acidic conditions, metal ions may leach from the solid catalysts, which can thus act as homogenous catalysts to improve pollutant degradation [19]. Under alkaline conditions, SO₄•⁻ may transform into •OH with lower degradation capacity [Eq.(4)], and SPS can be hydrolyzed to generate inert products such as SO₄²⁻, HSO₄⁻ and O₂ [Eqs.(5) and (6)] [22], thus resulting in the reduction of the degradation efficiency.

$$SO_4^{\bullet-} + H_2O \rightarrow SO_4^{2-} + H^+ + {}^\bullet OH \qquad (4)$$

$$S_2O_8^{2-} + H_2O \rightarrow 2HSO_4^- + \frac{1}{2}O_2 \qquad (5)$$

$$HSO_4^- \rightarrow SO_4^- + H^+ \qquad (6)$$
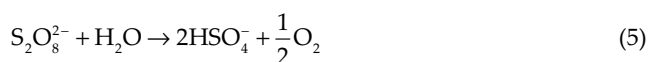
In this study, the pH_{zpc} of the three activators was found to be 4–5, meaning that at pH₀ < 4–5 the surface charges of the activators are positive and there would be negatively-charged when pH₀ > pH_{zpc}. On the other hands, the pKa value of MO is 3.8, so its molecules are charged positively and negatively at pH₀ < pKa and pH₀ > pKa, respectively. Under these conditions, the maximum adsorption of MO molecules could be obtained at pH values 4–5. Therefore, pH 4 was selected as a best value for subsequent tests of MO degradation.

3.6.4. Influence of reaction time

The influence of reaction time on MO removal using CuO/RGO, Fe₃O₄/RGO and CuFe₂O₄/RGO as activators in SR-AOPs was evaluated under the conditions of SPS dosage = 5 mM, activator dosage = 1.0 g/L, initial solution pH = 4. It can be found that MO removal proceeds very quickly in the initial 10 min (Fig. 7d). Specifically, 30%, 40% and 50% of MO is removed in the CuO/RGO, Fe₃O₄/RGO and CuFe₂O₄/RGO systems, respectively, after 10 min of reaction. Thereafter, the reaction rate gradually declines and reaches a plateau until the end. Actually, 100% MO is eliminated at 90 min in the CuFe₂O₄/RGO system, whereas the CuO/RGO and Fe₃O₄/RGO systems exhibit 82.5% and 78.6% removal efficiency at the same time (Fig. 7d). These results are in
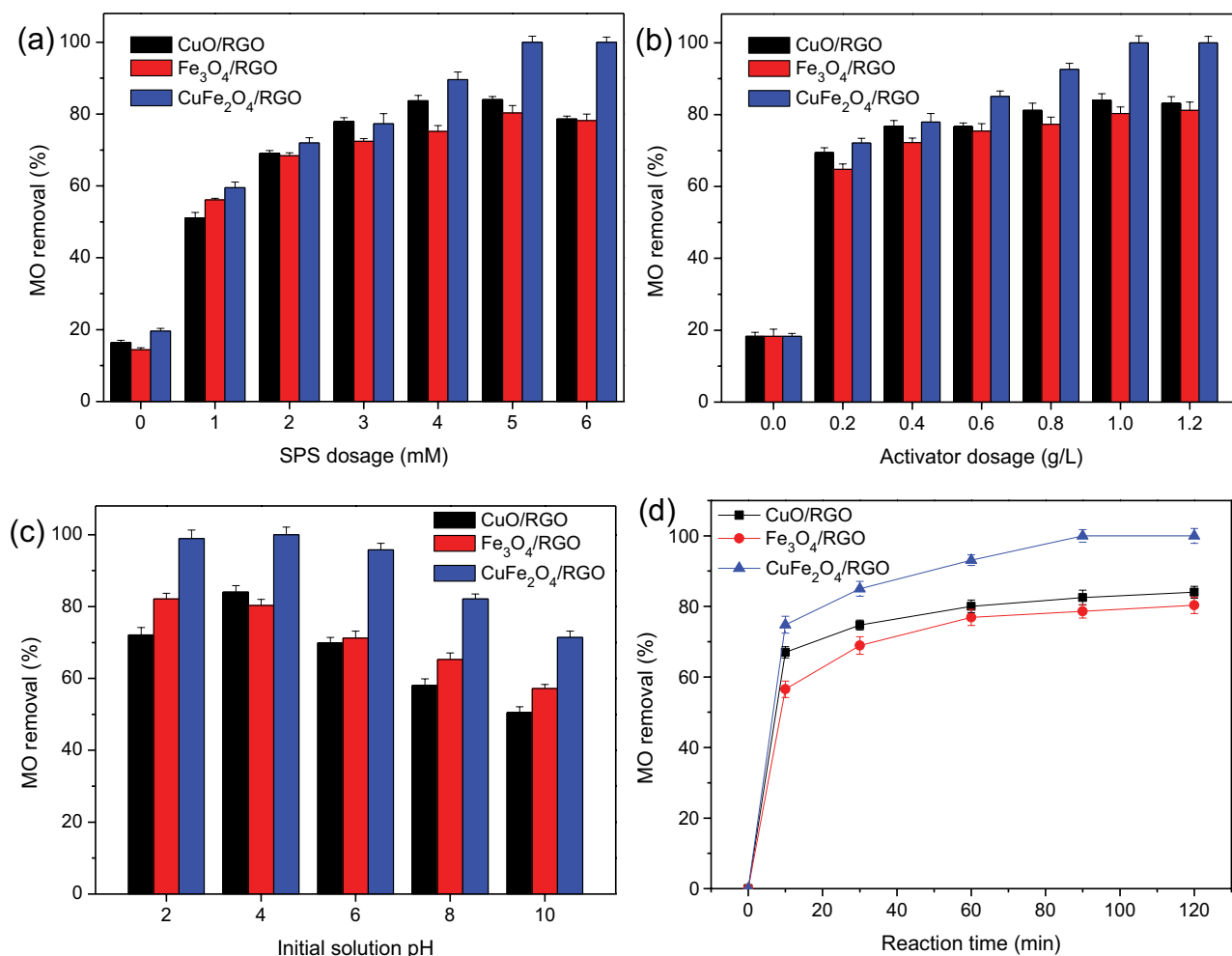
Fig. 7. Effect of reaction parameters on MO removal: SPS dosage (a), activator dosage (b), solution pH (c) and reaction time (d). (Reaction conditions: activator dosage = 1.0 g/L, initial solution pH = 4, reaction time = 120 min). The adsorption amounts of MO by the activators have been deducted from the data illustrated in (b), (c) and (d).

agreement with other reports [22,33,34]. In the initial stage of SR-AOPs, the concentrations of oxidants and pollutants are high, so a large amount of free radicals can be produced quickly which may fully contact and react with pollutants. As the reaction proceeds, the contents of oxidants and pollutants gradually decrease, thus their exposure opportunity gradually decreases. In addition, the active sites on the activator surface may be occupied by pollutants and their metabolites with the reaction going on. Therefore, after a certain duration, the reaction rate will gradually decline or even cease completely [4,32].

On the basis of the maximum value of MO removal efficiency over the investigated reaction parameters, the optimum conditions are SPS dosage = 5 mM, activator dosage = 1.0 g/L, initial solution pH = 4 and reaction time = 90 min for the $CuFe_2O_4$/RGO system. These conditions are also good for the CuO/RGO and Fe_3O_4/RGO systems. The above-mentioned results demonstrate that $CuFe_2O_4$/RGO NCs have higher activation capacity than CuO/RGO and Fe_3O_4/RGO NCs. This improved performance is attributed to the iron-copper synergy as reported previously [35,36].

3.7. Stability and reusability of activators

The reusability of persulfate activators is an important issue for their potential applications, which was evaluated through five consecutive reaction runs. As shown in Fig. 8a and b, in comparison with the initial cycle, the removal efficiency of MO decreases by 14.2 and 19.4% with 90 min after five sequential cycles in the CuO/RGO and Fe_3O_4/RGO systems, respectively. Comparatively, in the $CuFe_2O_4$/RGO system, MO removal remains at 90.2% with 90 min after five sequential cycles and exhibits a reduction of only 9.8% (Fig. 8c). These data confirms that the $CuFe_2O_4$/RGO NCs have adequate stability over the MO degradation and have a good application prospect in organic wastewater treatment by SR-AOPs due to its easy separation and excellent reusability. The decrease in activation capability of nano catalysts can be ascribed to [37]: (1) the overflow of metal ions on the catalysts; (2) the adsorption of reaction intermediates on the catalyst surface; and (3) the conglomeration of the catalysts during separation. To overcome these obstacles and enhance the activity of the used catalysts, they can be
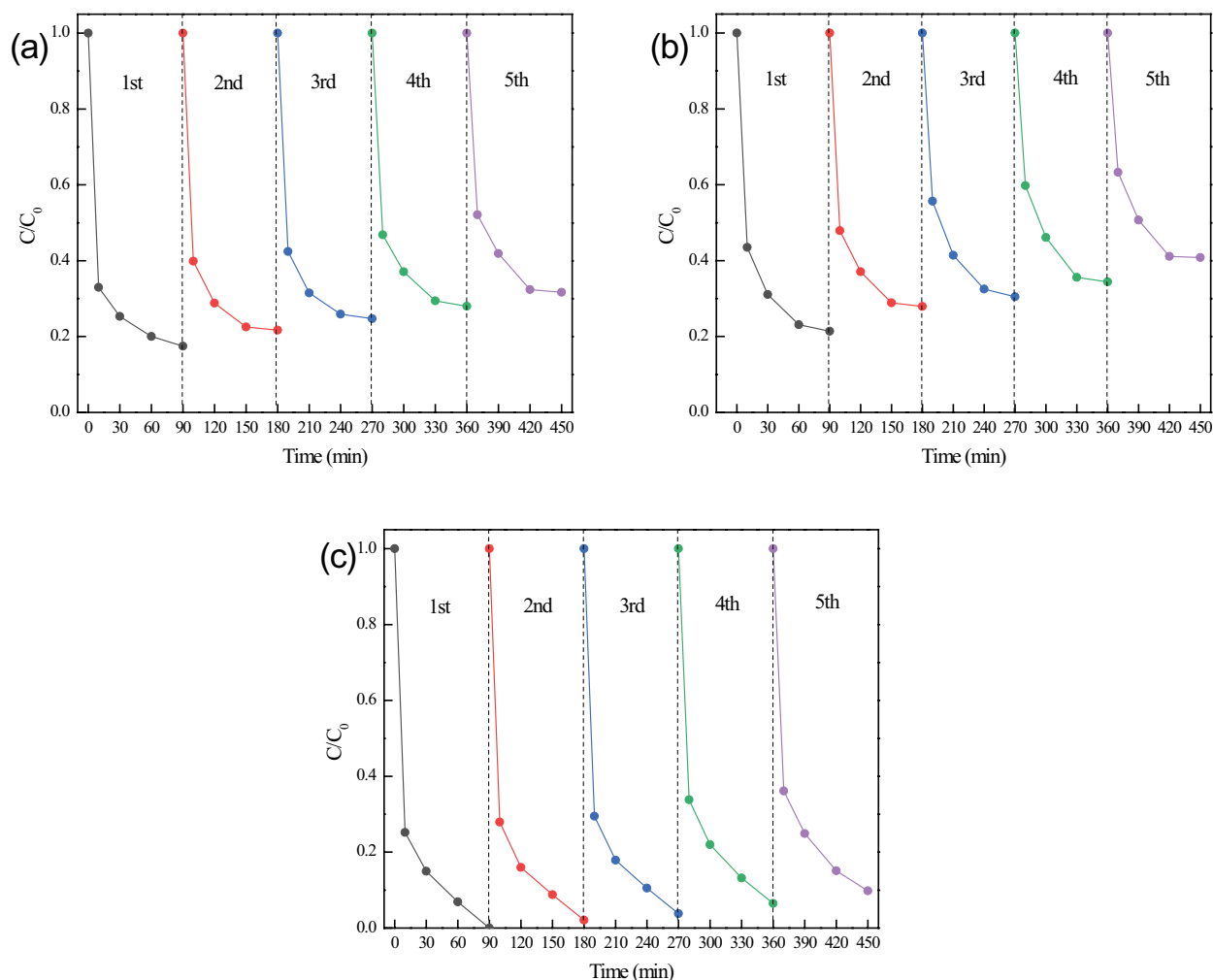
Fig. 8. Reusability of CuO/RGO (a), Fe_3O_4/RGO (b) and $CuFe_2O_4$/RGO (c) as activators activating SPS for MO degradation (C/C_o). (Reaction conditions: SPS dosage = 5 mM, activator dosage = 1.0 g/L, initial solution pH = 4).

calcined at high temperature (generally 400°C–500°C) to burn the adsorbed material and/or be subjected to ultrasonic treatment for reducing the catalyst conglomeration.

Table 1 shows the performance of several sulfate radical-based oxidation processes for dye removal. It can be found that the catalytic performance of pure Fe_3O_4 was moderate, while the complexation of iron oxides with other metals or non-metallic materials could significantly enhance the performance. The good performance of $LaFeO_3$ [38] and CuFe-LDH [39] was impressive, however the used catalysts were only separated by filtering due to its nonmagnetic property. In this study, $CuFe_2O_4$/RGO exhibited the advantages of both high catalytic activity and strong magnetism, verifying the good applicability of the material.

3.8. Free radical quenching experiments

Research shows that it contains α-hydrogen-containing MeOH can capture both $SO_4^{\bullet-}$ and $^\bullet OH$ at the reaction rate constants of 1.6–7.7×10^7 and 1.2–2.8×10^9 mol/L·s, respectively [40]. TBA without α-hydrogen has the reaction rate constant of 3.8–7.6×10^8 mol/L·s for $^\bullet OH$ which is far higher

than that for $SO_4^{\bullet-}$ (4–9.1×10^5 mol/L·s) [41]. Thus, MeOH scavenges effectively both $SO_4^{\bullet-}$ and $^\bullet OH$ while TBA is a strong scavenger for $^\bullet OH$. Fig. 9 illustrates the residue ratio of MO (C/C_0) in presence of MeOH or TBA as scavengers. As seen, in presence of MeOH or TBA, the C/C_0 value increases by 0.533 and 0.177, respectively, in comparison with the blank condition. Such difference suggests that $SO_4^{\bullet-}$ was the main responsible agent of MO degradation, and the contribution of $SO_4^{\bullet-}$ in reaction solution was higher than that of $^\bullet OH$ in the $CuFe_2O_4$/RGO system. The incomplete quenching at the later stage (Fig. 9) was possibly due to some other reactive species (e.g., $^1O_2$, $^\bullet O^{2-}$, H_2O_2, and $SO_5^{\bullet-}$) and direct oxidation of SPS [42].

4. Conclusions

In this work, CuO/RGO, Fe_3O_4/RGO and $CuFe_2O_4$/RGO NCs were successfully prepared by a one-step solvothermal method and these materials were characterized by various techniques such as XRD, XPS, SEM and FT-IR. The catalytic activity of the NCs was investigated for MO degradation in aqueous solution with SPS as the oxidant. $CuFe_2O_4$/

Table 1
Comparison between sulfate radical-based oxidation processes for dye removal

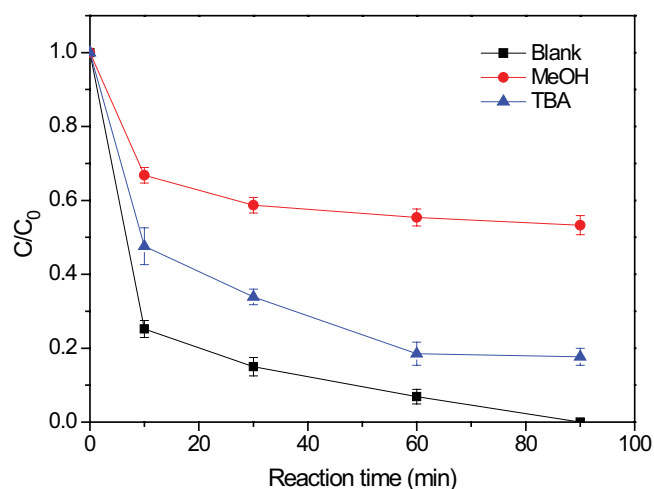| Reaction system	Reaction conditions	Dye removal	k_{obs}	Mineralization	Reference
α-Fe_2O_3	[pH]: 6.7 [persulfate]: 10 mM [catalyst]: 0.3 g/L [dye]$_0$:20 mg/L [time]: 30 min	100%	1.611×10^9 mol/L s	86.8%	[10]
Fe_3O_4	[pH]: 6.7 [persulfate]: 12 mM [catalyst]: 0.05 g/L [dye]$_0$: 0.02 mM [time]: 120 min	50%	0.01301 min^{-1}	–	[11]
$LaFeO_3$-visible light	[pH]: 8.07 [persulfate]: 3.552 mM [catalyst]: 1.0 g/L [dye]$_0$: 20 mg/L [time]: 180 min	100%	–	–	[38]
CuFe-LDH	[pH]: 5.6 [persulfate]: 0.2 g/L [catalyst]: 0.2 g/L [dye]$_0$: 20 mg/L [time]: 18 min	100%	0.202 min^{-1}	–	[39]
$CuFe_2O_4$/RGO	[pH]: 4.0 [persulfate]: 5 mM [catalyst]: 1.0 g/L [dye]$_0$: 50 mg/L [time]: 90 min	100%	–	–	This study

Fig. 9. The scavenging effect of MeOH and TBA on MO removal in the $CuFe_2O_4$/RGO system. (Reaction conditions: SPS dosage = 5 mM, activator dosage = 1.0 g/L, initial solution pH = 4).

RGO NCs showed higher MO removal levels compared to CuO/RGO and Fe_3O_4/RGO NCs under the optimal conditions and expanded the pH range, indicating a synergistic effect between iron and copper in SPS activation. Complete removal of MO was attained using the prepared $CuFe_2O_4$/RGO NCs within 90 min at room temperature. Moreover, the $CuFe_2O_4$/RGO NCs exhibited better reusability than CuO/RGO and Fe_3O_4/RGO NCs. Quenching experiments suggested that both $SO_4^{\bullet-}$ and $^{\bullet}OH$ were generated, but the former had a dominant position. All the results indicate that the $CuFe_2O_4$/RGO NCs are an efficient activator with good stability and reusability, which can be considered as a potential activator for the degradation of organic pollutants through SR-AOPs in aqueous solution. For the application of the catalyst in full scale, special attention should be paid to the persistence of catalyst surface activity in highly polluted water, because actual wastewater body may contain a variety of suspended solids and salts, which may be adsorbed on the catalyst surface, resulting in the masking of active sites and the declined catalytic activity.

Disclosure statement

No potential conflict of interest was reported by the authors.

Data availability statement

The data that support the findings of this study are available from the corresponding author Liu upon reasonable request.

References

[1] M.N. Khan, D.K. Parmar, D. Das, Recent applications of azo dyes: a paradigm shift from medicinal chemistry to biomedical sciences, Mini-Rev. Med. Chem., 21 (2021) 1071–1084.

[2] Aashima, S. Uppal, A. Arora, S. Gautam, S. Singh, R.J. Choudhary, S.K. Mehta, Magnetically retrievable Ce-doped Fe_3O_4 nanoparticles as scaffolds for the removal of azo dyes, RSC Adv., 9 (2019) 23129–23141.

[3] P. Aravind, H. Selvaraj, S. Ferro, M. Sundaram, An integrated (electro- and bio-oxidation) approach for remediation of industrial wastewater containing azo-dyes: understanding the degradation mechanism and toxicity assessment, J. Hazard. Mater., 318 (2016) 203–215.

[4] S. Giannakis, K.-Y.A. Lin, F. Ghanbari, A review of the recent advances on the treatment of industrial wastewaters by sulfate radical-based advanced oxidation processes (SR-AOPs), Chem. Eng. J., 406 (2021) 127083, doi: 10.1016/j.cej.2020.127083.

[5] H. Chi, J. Wan, Y. Ma, Y. Wang, S. Ding, X. Li, Ferrous metal–organic frameworks with stronger coordinatively unsaturated metal sites for persulfate activation to effectively degrade dibutyl phthalate in wastewater, J. Hazard. Mater., 377 (2019) 163–171.

[6] F. Ghanbari, M. Moradi, F. Gohari, Degradation of 2,4,6-trichlorophenol in aqueous solutions using peroxymonosulfate/activated carbon/UV process via sulfate and hydroxyl radicals, J. Water Process Eng., 9 (2016) 22–28.

[7] A.A. Babaei, M. Golshan, B. Kakavandi, A heterogeneous photocatalytic sulfate radical-based oxidation process for efficient degradation of 4-chlorophenol using TiO_2 anchored on Fe oxides@carbon, Process Saf. Environ. Prot., 149 (2021) 35–47.

[8] M. Noorisepehr, B. Kakavandi, A.A. Isari, F. Ghanbari, E. Dehghanifard, N. Ghomi, F. Kamrani, Sulfate radical-based oxidative degradation of acetaminophen over an efficient hybrid system: peroxydisulfate decomposed by ferroferric oxide nanocatalyst anchored on activated carbon and UV light, Sep. Purif. Technol., 250 (2020) 116950, doi: 10.1016/j.seppur.2020.116950.

[9] X. Li, Y. Jia, M. Zhou, L. Ding, X. Su, J. Sun, Degradation of diclofenac sodium by pre-magnetization Fe^0/persulfate system: efficiency and degradation pathway study, Water Air Soil Pollut., 231 (2020) 311, doi: 10.1007/s11270-020-04650-7.

[10] F. Meng, M. Song, B. Song, Y. Wei, Q. Cao, Y. Cao, Enhanced degradation of Rhodamine B via α-Fe_2O_3 microspheres induced persulfate to generate reactive oxidizing species, Chemosphere, 243 (2020) 125322, doi: 10.1016/j.chemosphere.2019.125322.

[11] Y. Leng, W. Guo, X. Shi, Y. Li, A. Wang, F. Hao, L. Xing, Degradation of Rhodamine B by persulfate activated with Fe_3O_4: effect of polyhydroquinone serving as an electron shuttle, Chem. Eng. J., 240 (2014) 338–343.

[12] N.K. Gupta, Y. Ghaffari, S. Kim, J. Bae, K.S. Kim, M. Saifuddin, Photocatalytic degradation of organic pollutants over MFe_2O_4 (M = Co, Ni, Cu, Zn) nanoparticles at neutral pH, Sci. Rep., 10 (2020) 4942, doi: 10.1038/s41598-020-61930-2.

[13] Mubasher, M. Mumtaz, M. Hassan, L. Ali, Z. Ahmad, M.A. Imtiaz, M.F. Aamir, A. Rehman, K. Nadeem, Comparative study of frequency-dependent dielectric properties of ferrites MFe_2O_4 (M = Co, Mg, Cr and Mn) nanoparticles, Appl. Phys. A, 126 (2020) 334, doi: 10.1007/s00339-020-03529-y.

[14] R. Dhanda, M. Kidwai, Magnetically separable $CuFe_2O_4$/reduced grapheme oxide nanocomposites: as a highly active catalyst for solvent free oxidative coupling of amines to imines, RSC Adv., 6 (2016) 53430–53437.

[15] W. Qin, G. Fang, Y. Wang, D. Zhou, Mechanistic understanding of polychlorinated biphenyls degradation by peroxymonosulfate

[16] V. Verma, M. Kaur, S. Sharma, Superoxide dismutase mimic activity of spinel ferrite MFe_2O_4 (M = Mn, Co and Cu) nanoparticles, Bull. Mater. Sci., 42 (2019) 120, doi: 10.1007/s12034-019-1783-7.

[17] S. Balamurugan, N. Naresh, I. Prakash, N. Satyanarayana, Ion and electron-conducting additive effect on Li-ion charge storage performance of $CuFe_2O_4$/SiO_2 composite aerogel anode, Ceram. Int., 46 (2020) 25330–25340.

[18] Y. Sohail, A. Liaquat, A. ul Haq, M.F. Zafar, N. Ul-Haq, Impedance spectroscopy and investigation of conduction mechanism in reduced graphene/$CuFe_2O_4$ nanocomposites, Appl. Physic. A, 127 (2021) 423, doi: 10.1007/s00339-021-04563-0.

[19] I. Othman, M.A. Haija, I. Ismail, J.H. Zain, F. Banat, Preparation and catalytic performance of $CuFe_2O_4$ nanoparticles supported on reduced graphene oxide ($CuFe_2O_4$/RGO) for phenol degradation, Mater. Chem. Phys., 238 (2019) 121931, doi: 10.1016/j.matchemphys.2019.121931.

[20] D. Karimipourfard, R. Eslamloueyan, N. Mehranbod, Novel heterogeneous degradation of mature landfill leachate using persulfate and magnetic $CuFe_2O_4$/RGO nanocatalyst, Process Saf. Environ. Prot., 131 (2019) 212–222.

[21] X. Ma, R. Hao, Z. Wang, P. Xu, Y. Luo, Y. Zhao, Nanoscale $CuFe_2O_4$ monodispersedly anchored on reduced graphene oxide as excellent peroxydisulfate catalyst for removal of gaseous elemental mercury, Chem. Eng. J., 401 (2020) 126101, doi: 10.1016/j.cej.2020.126101.

[22] P. Hao, M. Hu, R. Xing, W. Zhou, Synergistic degradation of methylparaben on $CuFe_2O_4$-rGO composite by persulfate activation, J. Alloys Compd., 823 (2020) 153757, doi: 10.1016/j.jallcom.2020.153757.

[23] D.C. Marcano, D.V. Kosynkin, J.M. Berlin, A. Sinitskii, Z.Z. Sun, A. Slesarev, L.B. Alemany, W. Lu, J.M. Tour, Improved synthesis of graphene oxide, ACS Nano, 4 (2010) 4806–4814.

[24] U. Holzwarth, N. Gibson, The Scherrer equation versus the 'Debye-Scherrer equation', Nat. Nanotechnol., 6 (2011) 534, doi: 10.1038/nnano.2011.145.

[25] H. Gu, X. Chen, F. Chen, X. Zhou, Z. Parsaee, Ultrasound-assisted biosynthesis of CuO-NPs using brown alga *Cystoseira trinodis*: characterization, photocatalytic AOP, DPPH scavenging and antibacterial investigations, Ultrason. Sonochem., 41 (2018) 109–119.

[26] M. Bagavathi, A. Ramar, R. Saraswathi, Fe_3O_4–carbon black nanocomposite as a highly efficient counter electrode material for dye-sensitized solar cell, Ceram. Int., 42 (2016) 13190–13198.

[27] H. Dai, S. Xu, J. Chen, X. Miao, J. Zhu, Oxalate enhanced degradation of Orange II in heterogeneous UV-Fenton system catalyzed by Fe_3O_4@γ-Fe_2O_3 composite, Chemosphere, 199 (2018) 147–153.

[28] X. Wang, J. Min, S. Li, X. Zhu, X. Cao, S. Yuan, X. Zuo, X. Deng, Sono-assisted synthesis of CuO nanorods–graphene oxide as a synergistic activator of persulfate for bisphenol A removal, J. Environ. Chem. Eng., 6 (2018) 4078–4083.

[29] M.F. Li, Y.G. Liu, S.B. Liu, D. Shu, G.M. Zeng, X.J. Hu, X.F. Tan, L.H. Jiang, Z.L. Yan, X.X. Cai, Cu(II)-influenced adsorption of ciprofloxacin from aqueous solutions by magnetic graphene oxide/nitrilotriacetic acid nanocomposite: competition and enhancement mechanisms, Chem. Eng. J., 319 (2017) 219–228.

[30] X. Zhang, M. Feng, R. Qu, H. Liu, L. Wang, Z. Wang, Catalytic degradation of diethyl phthalate in aqueous solution by persulfate activated with nano-scaled magnetic $CuFe_2O_4$/MWCNTs, Chem. Eng. J., 301 (2016) 1–11.

[31] S. Madihi-Bidgoli, S. Asadnezhad, A. Yaghoot-Nezhad, A. Hassani, Azurobine degradation using Fe_2O_3@multi-walled carbon nanotube activated peroxymonosulfate (PMS) under UVA-LED irradiation: performance, mechanism and environmental application, J. Environ. Chem. Eng., 9 (2021) 106660, doi: 10.1016/j.jece.2021.106660.

[32] L.W. Matzek, K.E. Carter, Activated persulfate for organic chemical degradation: a review, Chemosphere, 151 (2016) 178–188.

[33] S.S. Rezaei, B. Kakavandi, M. Noorisepehr, A.A. Isari, S. Zabih, P. Bashardoust, Photocatalytic oxidation of tetracycline by magnetic carbon-supported TiO_2 nanoparticles catalyzed peroxydisulfate: Performance, synergy and reaction mechanism studies, Sep. Purif. Technol., 258 (2021) 117936, doi: 10.1016/j.seppur.2020.117936.

[34] M. Moradi, B. Kakavandi, A. Bahadoran, S. Giannakis, E. Dehghanifard, Intensification of persulfate-mediated elimination of bisphenol A by a spinel cobalt ferrite-anchored g-C3N4 S-scheme photocatalyst: catalytic synergies and mechanistic interpretation, Sep. Purif. Technol., 285 (2022) 120313, doi: 10.1016/j.seppur.2021.120313.

[35] Z. Li, C. Guo, J. Lyu, Z. Hu, M. Ge, Tetracycline degradation by persulfate activated with magnetic $Cu/CuFe_2O_4$ composite: efficiency, stability, mechanism and degradation pathway, J. Hazard. Mater., 373 (2019) 85–96.

[36] Y. Ren, J. Yu, J. Zhang, L. Lv, W. Zhang, An in-situ strategy to analyze multi-effect catalysis in iron-copper bimetals catalyzed Fenton-like processes, Appl. Catal., B, 299 (2021) 120697, doi: 10.1016/j.apcatb.2021.120697.

[37] Q. Ma, H. Zhang, X. Zhang, B. Li, R. Guo, Q. Cheng, X. Cheng, Synthesis of magnetic $CuO/MnFe_2O_4$ nanocompisite and its high activity for degradation of levofloxacin by activation of persulfate, Chem. Eng. J., 360 (2019) 848–860.

[38] W. Meng, Y. Wang, Y. Zhang, C. Liu, Z. Wang, Z. Song, B. Xu, D.C.W. Tsang, F. Qi, A. Ikhlaq, Degradation Rhodamine B dye wastewater by sulfate radical-based visible light-Fenton mediated by $LaFeO_3$: reaction mechanism and empirical modeling, J. Taiwan Inst. Chem. Eng., 111 (2020) 162–169.

[39] Y. Ma, F. Chen, Q. Yang, Y. Zhong, X. Shu, F. Yao, T. Xie, X. Li, D. Wang, G. Zeng, Sulfate radical induced degradation of Methyl Violet azo dye with CuFe layered doubled hydroxide as heterogeneous photoactivator of persulfate, J. Environ. Manage., 227 (2018) 406–414.

[40] Y. Xu, J. Ai, H. Zhang, The mechanism of degradation of bisphenol A using the magnetically separable $CuFe_2O_4$/peroxymonosulfate heterogeneous oxidation process, J. Hazard. Mater., 309 (2016) 87–96.

[41] J. Peng, Z Wang, S. Wang, J. Liu, Y. Zhang, B. Wang, Z. Gong, M. Wang, H. Dong, J. Shi, H. Liu, G. Yan, G. Liu, S. Gao, Z. Cao, Enhanced removal of methylparaben mediated by cobalt/carbon nanotubes (Co/CNTs) activated peroxymonosulfate in chloride-containing water: reaction kinetics, mechanisms and pathways, Chem. Eng. J., 409 (2021) 12817, doi: 10.1016/j.cej.2020.128176.

[42] Y. Qi, J. Wei, R. Qu, G. Al-Basher, X. Pan, A.A. Dar, A. Shad, D. Zhou, Z. Wang, Mixed oxidation of aqueous nonylphenol and triclosan by thermally activated persulfate: reaction kinetics and formation of co-oligomerization products, Chem. Eng. J., 403 (2021) 126396, doi: 10.1016/j.cej.2020.126396.